



Research Paper

Zinc vacancy-promoted photocatalytic activity and photostability of ZnS for efficient visible-light-driven hydrogen evolution



Xuqiang Hao, Yicong Wang, Jun Zhou, Zhiwei Cui, Ying Wang*, Zhigang Zou*

Eco-Materials and Renewable Energy Research Center (ERERC), School of Chemistry and Chemical Engineering, National Laboratory of Solid State Microstructures, Kunshan Innovation Institute of Nanjing University, Jiangsu Key Laboratory for Nanotechnology, Nanjing, 210023, PR China

ARTICLE INFO

Keywords:

ZnS
Zinc vacancies
Defect states
Visible-light response
Photocatalytic hydrogen evolution

ABSTRACT

Zinc sulfide is a superior photocatalyst for H₂ evolution, whereas the wide bandgap restricts its performance to only UV region. In this work, zinc vacancy (V_{Zn}) defects are successfully introduced into ZnS via adding sodium sulfide as sulfur source during the hydrothermal reaction. The defective ZnS with different amount of zinc vacancies were employed as catalysts for the examination of vacancy-dependent catalytic activity toward photocatalytic hydrogen evolution under visible light irradiation. Fluorescence emission spectra and XPS results confirm that existence of abundant zinc vacancies on ZnS. These zinc vacancies exhibit remarkable effects on modifying the electronic structure of ZnS as shown in UV-visible absorption spectra and Mott-Schottky plots. Zinc vacancies can raise valence band (VB) position that weaken the oxidative capacity of the holes to protect Zn-deficient ZnS from photocorrosion. And electrochemical and photo-electrochemical experiments also demonstrate that the charge separation and the electrons transfer are more efficient with the introduction of the Zn vacancies in ZnS. The zinc-deficient ZnS-2.5 with optimum amount of Zn vacancies shows superior photocatalytic activity for H₂ evolution that reaches 337.71 ± 3.72 μmol h⁻¹ g⁻¹ under visible-light irradiation and also exhibits a much higher photostability. The intrinsic modify by self-defects might be a potential strategy for design novel photocatalysts with photocorrosion stability and visible-light activity in photocatalysis proton reduction.

1. Introduction

Photocatalytic hydrogen evolution from water splitting using semiconductor materials for solar conversion has been considered as a desirable approach with clean, environmentally friendly and economical process [1–3]. In the past few decades, numerous efforts have been taken to develop suitable semiconductor photocatalysts to obtain high activities for water splitting [3–7]. However, major limitations to achieve high photocatalytic efficiency using solar energy are restricted by the light absorption and the fast recombination of electron-hole pairs [8]. Common semiconductors, such as TiO₂ and ZnO, mainly absorb UV light, which means they use only about 4% of the solar spectrum [9]. And there is still not finding an ideal photocatalyst for practical use with relatively high productivity under visible light. Therefore, it is important to develop a robust photocatalyst that can efficiently utilize visible light for hydrogen production.

ZnS is a promising n-type semiconductor for photocatalytic hydrogen production due to its rapidly generates photoexcited electron-hole pairs, and high activity under UV light [10,11]. Unfortunately, the photocatalytic performance of pristine ZnS is restricted by its wide band

gap (3.6–3.8 eV), which means that ZnS is only active under UV light and not respond to visible light [9]. Therefore, several attempts have been made to extend the light absorption of ZnS into the visible region for photocatalytic H₂ evolution, such as doping [12–19], coupling with metals sulfide [20,21], structure engineering [22], hybridization [23,24] and so on. For example, it is reported that introducing extrinsic metal elements (Cu, Ni, Cd,...) or nonmetal elements (C, N) to ZnS for enhancing the visible light photocatalysis [13–21]. However, compared with these efforts, the intrinsic modification of ZnS by self-defects for visible-light photocatalytic H₂ evolution are rarely reported.

As is known, the intrinsic nature of materials, such as defect states, crystalline phases, exposed facets, etc., of semiconductor photocatalysts are crucial factors for superior photocatalytic activities, which can regulate the light absorption behavior for robust charge generation, dominate the kinetics of charge transfer for effective charge separation, and organize active sites or facets for charge utilization [22]. Thus, it is of significance to understand the effect of intrinsic properties on ZnS to enhance its visible light photocatalysis. Among these nature of materials, defect engineering is an appealing strategy for enhancing light harvesting in photocatalytic materials [25]. Defects in semiconductor

* Corresponding authors.

E-mail addresses: wangy@nju.edu.cn (Y. Wang), zgzou@nju.edu.cn (Z. Zou).

photocatalysts not only can introduce new energy levels to narrow the band gap that produce visible-light activity, but also can serve as adsorption sites where the charge transfer and prevent the recombination of photogenerated charge carriers. It is worth noting that controlling the amount of defects is great important to photocatalytic reaction, because excessive amount defects can act as recombination centers for charge carriers and hence decreasing the photocatalytic activity. Vacancy defects can play an important role in modifying the electronic structure and the properties of photoexcited charge carriers by introducing additional energy levels and consequently enhanced the photocatalytic activity of photocatalyst. For example, oxygen vacancies are one of kind of intrinsic defects in crystals, which have been found to play a crucial role in TiO_2 [26,27], ZnO [28,29], Fe_2O_3 [30], BiOCl [31] photocatalysts for improving visible-light photocatalytic response. Furthermore, the nitrogen vacancies also can significantly redshift the absorption edge of $\text{g-C}_3\text{N}_4$ with superior visible-light photocatalytic performance compared to pristine $\text{g-C}_3\text{N}_4$ [32–35]. Recently, it is reported that S vacancies in ZnS can induce an excellent photocatalytic activity for H_2 production under visible light [22,36]. And the photocatalytic activity of ZnS increases steadily with increasing the concentration of S vacancies, which can serve as photosensitization units that induce visible light response and as active sites that trap electrons for proton reduction [22]. Moreover, the Zn vacancies (V_{Zn}) are also beneficial to modify the light absorption behavior and narrow the bandgap of ZnS film for photocatalysis under visible-light irradiation. It is reported that the Zn-deficient ZnS film with a band gap of ~ 2.4 eV was fabricated by pulsed laser deposition (PLD) by control the N_2 background pressure. It exhibits a high photocurrent density of 1.5 mA cm^{-2} under visible light irradiation ($\lambda \geq 435 \text{ nm}$) [37]. Most recently, ZnS nanoparticles were prepared using ultrasonic methods with Zn vacancy and interstitial sulfur states, exhibited more outstanding photocorrosion stability and photocatalytic activity for degrading reactive black 5 (RB5) under visible light irradiation [38]. These results clearly indicate Zn vacancies engineering is a potential approach for regulate the light absorption behavior and photostability in photocatalysis. However, each of these approaches to prepare zinc deficient ZnS has inherent limitations (low crystallinity, cannot large-scale preparation, etc.) and affords limited control over the type and abundance of zinc defect that they can introduce. And also, there has no systematically research on Zn vacancies in ZnS with an aim for photocatalytic hydrogen evolution under visible light irradiation. Therefore, it is desirable to develop a facile approach for introducing zinc vacancy into ZnS with an enhanced visible-light photocatalytic response and photocatalytic corrosion resistant for hydrogen evolution.

In this work, we report a facile hydrothermal strategy to introduce zinc vacancies in the ZnS structure via adding sodium sulfide (Na_2S) as sulfur source. The zinc-deficient ZnS -2.5 with optimum amount of Zn vacancies can be as an efficient photocatalyst for H_2 production operating under visible-light irradiation. The effects of zinc vacancy-related properties on the visible-light photocatalytic activity of ZnS are investigated. The prepared zinc-deficient ZnS samples exhibit enhanced visible-light absorption with increasing the amount of zinc vacancies, which can be easily controlled by varying amount of Na_2S used during the hydrothermal reaction. Furthermore, the introduction of zinc vacancies serve as defects energy levels above the valence band (VB) in ZnS , which act as an acceptor levels for the photoinduced holes that improve charge carrier separation rate and weaken the oxidative capacity of the holes to protect Zn-deficient ZnS from photocorrosion. This work highlights the critical role of defects in the wide-bandgap metal sulfide photocatalysts for optimizing the optical response, and photocatalytic performance.

2. Experimental

All the chemicals in the experiments were of analytical reagent grade and used without further purification.

2.1. Synthesis of zinc-deficient ZnS photocatalysts

ZnS photocatalysts with different molar ratio of Zn/S were prepared by a one-pot hydrothermal method. Typically, 10 mmol $\text{Zn}(\text{Ac})_2 \cdot 2\text{H}_2\text{O}$ with diffident molar ratio of $\text{Na}_2\text{S} \cdot 9\text{H}_2\text{O}$ was dissolved in 30 mL deionized water to form a white slurry solution under magnetic stirring condition at room temperature. After stirring for 60 min, the white slurry precursor solution was then transferred into a 50 mL Teflon-lined autoclave and maintained at 200 °C for 20 h. Finally, the grey white precipitate was obtained by centrifugation and washed several times with deionized water and ethanol and vacuum dried at 60 °C overnight. The molar ratio of $\text{Zn}(\text{Ac})_2 \cdot 2\text{H}_2\text{O}$ to $\text{Na}_2\text{S} \cdot 9\text{H}_2\text{O}$ was fixed as 1:1, 1:1.5, 1:2, 1:2.5, 1:3 (namely, molar ratio Zn/S = 1:1, 1:1.5, 1:2, 1:2.5, 1:3) and obtained products were named as ZnS-X , that is, ZnS-1 , ZnS-1.5 , ZnS-2 , ZnS-2.5 , ZnS-3 , respectively.

2.2. Characterizations

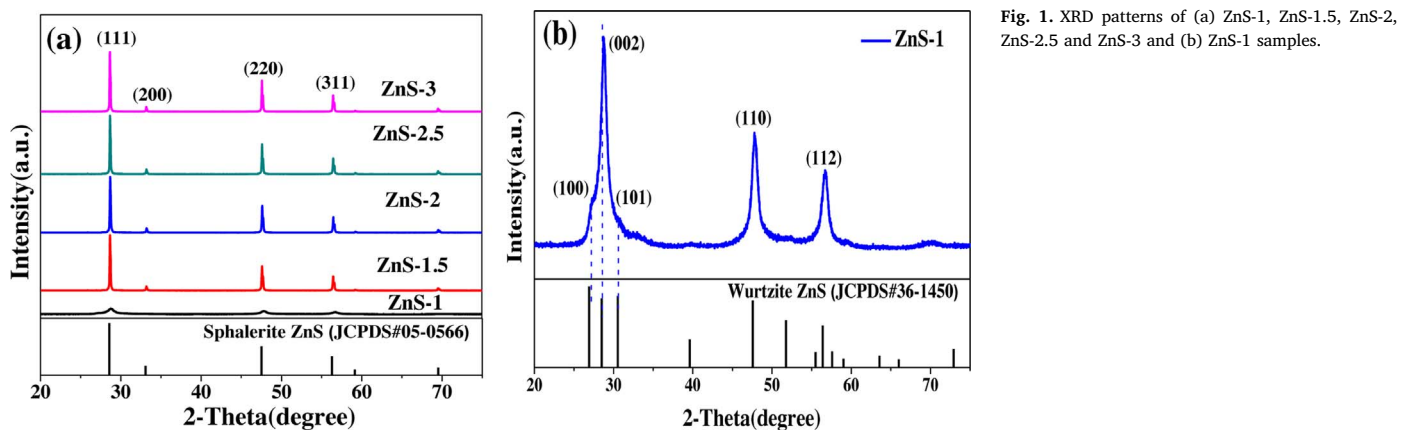
Powder X-ray diffraction (PXRD) data were collected using a Rigaku Ultima III X-ray diffractometer using Cu K α radiation ($\lambda = 1.54056 \text{ \AA}$). Scanning electron microscope (SEM) images were recorded with a Hitachi S4800 FE-SEM system. Transmission electron microscope (TEM) and high-resolution transmission electron microscope (HRTEM) images were obtained by using a JEM-2100 electron microscope. Visible Raman spectra were recorded on a Horiba confocal LabRAM Aramis spectrometer using a 532 nm single-frequency excitation laser. Chemical states of the obtained samples were characterized by a PHI 5000 Versa Probe X-ray photoelectron spectrometer (a monochromatic Al Ka X-ray radiation). All of the binding energies of all elements were calibrated by the C 1s peak at 284.6 eV. UV-vis spectra were collected using a Shimadzu UV-3600 spectrometer, BaSO_4 was used as reference. The photoluminescence (PL) spectra were taken on a Varian Cary Eclipse Fluorescence spectrometer with an excitation wavelength of 320 nm. The Zn content for ZnS samples were analyzed by chemical titration and the detailed experiment can be seen in supporting information.

2.3. Photocatalytic hydrogen evolution

The photocatalytic hydrogen evolution reactions were conducted in a side-irradiation Pyrex reactor, which connected to a glass-closed gas circulation system at ambient temperature. In a typical photocatalytic experiment, 50 mg of catalyst power was suspended in 400 mL aqueous solution containing Na_2S and Na_2SO_3 as the sacrificial agent of the hole. Before visible light irradiation, the reactant system was degassed by evacuation to remove air and ensure that the reaction system was under anaerobic conditions, and then was irradiated by a 300-W Xe lamp with a cutoff filter of 420 nm for H_2 evolution under magnetic stirring condition. The amount of hydrogen evolution was analyzed by an online gas chromatograph (GC-14C, Shimadzu, TCD, Ar as carrier).

2.4. Electrochemical measurements

The photoelectrochemical measurement was performed on an electrochemical analyzer (Chenhua CHI 660D) in a standard three-electrode cell. The working electrodes were prepared by drop-coating homogeneous catalyst suspensions directly onto the precleaned indium tin oxide glass (ITO glass) surfaces ($1 \times 2 \text{ cm}$). Platinum wire was used as the counter electrode, and a saturated calomel electrode (SCE) was used as the reference electrode. $E^\circ = 0.241 \text{ V vs. NHE}$ at 25 °C for saturated calomel electrode. Na_2SO_4 (0.5 M, pH = 0.68) aqueous solution was used as supporting electrolyte. The Mott–Schottky curves were taken under dark with a voltage of 5 mV at three frequencies of 1.0, 1.5 and 2.0 kHz, respectively. The potential ranged from -1.7 to 1.0 V (vs. SCE). Electrochemical impedance spectroscopy (EIS) plots were collected at open circuit potential (0.5 V vs. SCE), with the frequency



ranging from 100 kHz to 0.01 Hz and the modulation amplitude of 5 mV. The transient photocurrent measurements were recorded at an applied potential of 0.5 V vs. SCE under the visible light illumination. A 300-W Xe lamp equipped with an optical cutoff filter of 420 nm was employed for the visible-light excitation. The electrocatalytic activity of the samples were examined by obtaining polarization curves using linear sweep voltammetry (LSV) with a scan rate of 5 mV s⁻¹ at room temperature.

3. Results and discussion

3.1. Characterization of catalysts

3.1.1. XRD analysis

Fig. 1a shows the XRD patterns of ZnS-X photocatalysts with different molar ratio of Zn/S. It can be seen that the as-prepared ZnS-1.5, ZnS-2, ZnS-2.5 and ZnS-3 have the similar diffraction peaks, the sharp peaks of these samples indicate its excellent crystallinity, and all the peak can well matched with the sphalerite ZnS (JCPDS#05-0566). And there is no other peaks can be observed, indicating it is a pure ZnS. It is noteworthy that the diffraction peaks of ZnS-1 are weaker than other four samples, suggesting its relative lower crystallinity. Fig. 1b shows the XRD pattern of ZnS-1 alone, five characteristic peaks at 27.12°, 28.55°, 30.62°, 47.75° and 56.69° belong to (100), (002), (101), (110) and (112) plane fit well with wurtzite-2H ZnS (JCPDS#36-1450). Intriguingly, crystal phase transformation of ZnS-1 from sphalerite to wurtzite after hydrothermal treatment (Fig. S1a), while this phase transform phenomenon no longer occurs on the samples with an increasing amount of Na₂S in precursor solution at the identical hydrothermal temperature, such as ZnS-2.5 (Fig. S1b). To our best knowledge, this is first report about the phase structure transform of ZnS with varying amount of Na₂S in precursor solution. It is known that the cubic (sphalerite) phase of ZnS is stable at room temperature whereas the hexagonal (wurtzite) phase is a high-temperature form that exists above 1020 °C. However, the phase stability can be significantly affected by the particle size, cubic ZnS may transform into hexagonal ZnS at temperatures much lower than 1020 °C for nanoscale ZnS [39]. It is reported that crystal growth of wurtzite is kinetically controlled by the radius of the sphalerite-wurtzite interface and crystal growth of wurtzite stops when the diameter of the sphalerite-wurtzite interface reaches ~22 nm [40]. The size-dependent phase transformation kinetics maybe used to understand the phase structure transformation of cubic ZnS to hexagonal ZnS [40]. According to the Debye-Scherrer formula ($D = K\lambda/(\beta \cos \theta)$), the particle size of ZnS-1 is small as 3.52 nm before hydrothermal treatment and grown into 6.31 nm on the basis of (002) peak. We can infer that there is not have excess of S²⁻ to support it grow into big size in the process of Ostwald-ripening, so the phase transformation of sphalerite to wurtzite occurred. With increasing amount of Na₂S in precursor solution, the average crystallite

size speedily increased for ZnS-2.5 from 6.78 nm to 65.92 nm. The high concentration of Na₂S affords a larger driving force that accelerate the speed of smaller size crystals growth into large size during the ripening process and the size is much greater than the diameter of the sphalerite-wurtzite interface of 22 nm, so the phase transform phenomenon no longer occurs when continue to increase the amount of Na₂S in precursor solution. This implies that the low concentration of Na₂S has a structure-oriented effect in the chemically induced self-transformation process of ZnS crystals.

3.1.2. Raman characterization

The surface phase structure of representative ZnS-1 and ZnS-2.5 samples are further differentiated by visible Raman spectroscopy. As shown in Fig. 2, Raman spectra of ZnS-1 has a strong peak in the 349.79 cm⁻¹ after magnify 15 times, which can be attributed to longitudinal-optic A1(LO) and E1(LO) phonon mode of wurtzite ZnS [41], While the scattering peak at 267.81 cm⁻¹ is derived from the transverse optical vibration mode (TO) of wurtzite ZnS [42]. The broad weak peak at 402.35 cm⁻¹ can be assigned to transverse acoustic and optical modes (TA + TO) along the M-L-H line and the peak at 498.73 cm⁻¹ is the TO mode of the Si substrate. As for ZnS-2.5, T₂(TO) and T₂ (LO) modes near the Brillouin zone (ZB) center are located at 280.37 and 355.07 cm⁻¹, which are very close to the previous reported for sphalerite ZnS [43]. Compared with that in the spectrum of ZnS-1, the peak at 355.07 cm⁻¹ is special sharp and strong, which can be attributed to the highly crystallinity. In the high-frequency region, there are three main modes at 619.88, 644.63 and 675.88 cm⁻¹, the first two can be assigned to the 2TO overtones, while the last is subject to 2(LO). In the

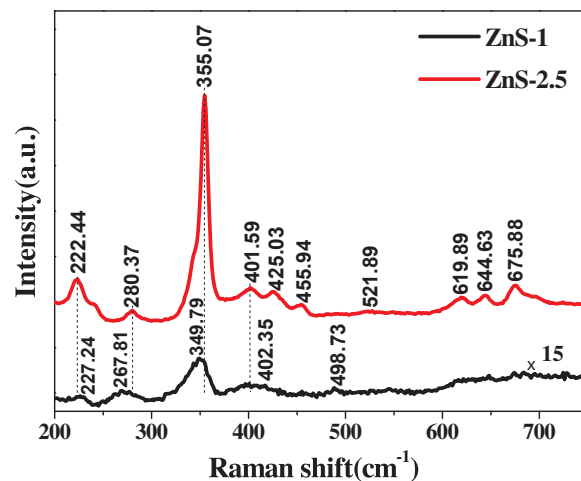
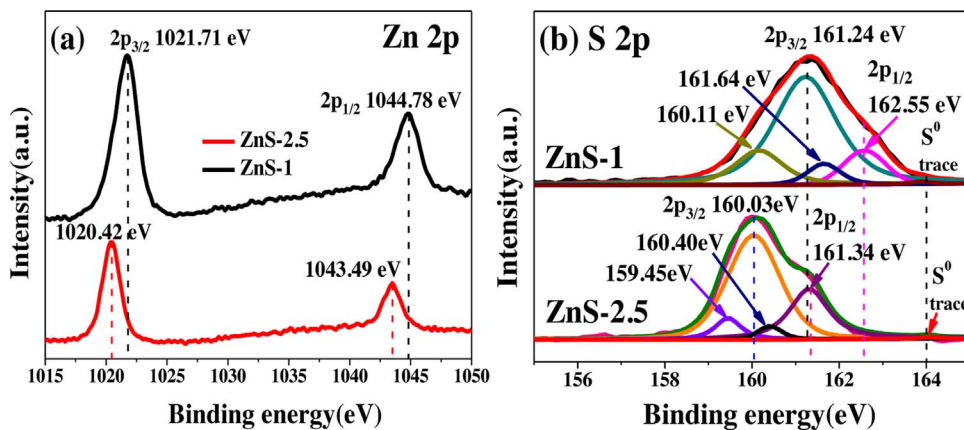


Fig. 2. Raman spectra of representative ZnS-1 and ZnS-2.5 samples with excitation line at 532 nm.



intermediate-frequency region, we can assign the combination band at 401.59, 425.03 and 459.94 cm⁻¹ to transverse optical and longitudinal acoustic mode (TO + LA) at X, L, W of BZ points, respectively [43]. The mode at 521.89 cm⁻¹ is the TO mode of the Si substrate [43]. What's more, no other peak beyond ZnS can be observed, indicating ZnS-1 and ZnS-2.5 are pure phase. The Raman spectra results are well agreement with XRD, which further suggesting the phase structure of the ZnS-1 and ZnS-2.5 samples.

3.1.3. X-ray photoelectron spectroscopy (XPS)

With a view to further ascertain the details of the surface chemical composition and valence state of the ZnS sample, the XPS spectra of the ZnS-1 and ZnS-2.5 were measured. The XPS survey spectrum, as depicted in Fig. S2, revealing that the catalyst is mainly consist of Zn, S, C and O elements. The C 1s at 284.6 eV was used as a reference to correct the binding energies. In Fig. 3a, the high-resolution XPS spectra of Zn 2p for ZnS-1 shows two peaks at 1044.78 eV and 1021.71 eV, which are assigned to Zn 2p_{1/2} and Zn 2p_{3/2} respectively [44]. Compared to the ZnS-1, the binding energies of Zn 2p_{1/2} and Zn 2p_{3/2} for ZnS-2.5 at 1043.53 eV and 1020.52 eV shift about 1.16 and 1.13 eV toward lower binding energy, respectively. From the high resolution S2p XPS spectrum of ZnS-1 (Fig. 3b), the peak at 161.24 eV is ascribed to S 2p_{3/2}, while the peak at 162.55 eV could be assigned to S 2p_{1/2}. In comparison, with increasing the amount of Na₂S during the synthesis, the binding energy for the Zn 2p and S 2p of the ZnS-2.5 sample shift gradually to a lower energy. This is attributed to the presence of defect states in ZnS structure [36,37]. While the binding energy of S 2p_{3/2} and S 2p_{1/2} shift toward lower binding energy to 160.03 eV and 161.34 eV in the S2p spectrum of ZnS-2.5, decrease by 1.21 eV. It is reasonable to deduce that the peaks of those S²⁻ ions are adjacent to the Zn vacancy sites that are single negative charge states, leading to an increase in the electronic density around the Zn vacancy sites and decrease the binding energies of the S²⁻ ions. Furthermore, two additional peaks appear for S 2p both in ZnS-1 and ZnS-2.5 at lower binding energies, further indicating that the existence of the defect states in the ZnS structure [37]. In addition, much weak peak attributed to elemental sulfur (S⁰) are observed in Fig. 3b and d for both ZnS-1 (163.89 eV) and ZnS-2.5 (164.05 eV) [18], implying that there are traces of S⁰ in the ZnS. These elemental sulfur (S⁰) maybe originated from the Na₂S oxidation by dissolved oxygen in the process of hydrothermal reaction. The XPS quantitative analysis results of Zn:S atomic ratio for ZnS-X are listed in

Table 1
The chemical composition of ZnS-1 and ZnS-2.5 measured by XPS.

Samples	Zn (at.%)	S (at.%)	Zn:S
ZnS-1	0.38	0.62	0.61:1
ZnS-2.5	0.28	0.72	0.39:1

Table 1 in detail. The Zn:S atomic ratio of ZnS-1 and ZnS-2.5 are 0.61:1 and 0.39:1, respectively, both are lower than their stoichiometry Zn:S atomic ratio of 1:1. It is interesting to note that Zn defects increase as the increase of sulfur precursor. Considering the XPS technique merely gives the surface information of the samples, we measured the component of bulk ZnS-X by chemical compolexmetric titration and summarized the results in Table S1. The data revealed that, as expected, the bulk Zn:S mole ratio of ZnS-1 and ZnS-2.5 are higher than XPS analysis result, indicating the Zn defects are located in surface layer. This implies that the surface concentration of Zn deficient can be controlled by varying the amount of Na₂S used in the precursor solution to a certain degree.

3.1.4. Photoluminescence (PL) analysis

To further prove the existence of Zn vacancy or other defects in ZnS, the photoluminescence emissions of the ZnS-X solid powder samples were performed. As shown in Fig. 4a, all the ZnS-X catalysts excited at 320 nm show a typically intrinsic emission peak at 377 nm, and a shoulder peak at 407 nm is due to surface states [45]. Notably, a broad peak consist of several small PL peaks are observed at wavelength of 430–630 nm region, this broad emission peak shifts toward long wavelength for the samples with Zn:S mole ratio larger than 1:1, and the strongest emission intensity was obtained on ZnS-2.5. It is likely that these small peaks are due to the existence of defects in the structure of ZnS. The defect emission was reported to associate with the point defects which serve as luminescent sites during photoluminescence processes [38]. Generally, there are four types of point defects can exist in pure ZnS: sulfur vacancies (V_S), zinc vacancies (V_{Zn}), interstitial sulfur atoms (I_S) and interstitial zinc atoms (I_{Zn}) [38]. In order to more clearly observed, the region of 430 ~ 630 nm of the represented ZnS-1 and ZnS-2.5 are depicted in Fig. 4b. As shown in the spectrum of ZnS-1, there is seven weak peaks are observed, which are located in the 448, 460, 488, 528, 545, 588 and 618 nm. The peaks around 448, 460 and 528 nm can be attributed to the point defects produced by zinc vacancies [45–48], which are derived from the conduction band (CB) electrons radiation transition to the single negative charge state Zn vacancy (V_{Zn}⁻). The peak at 488, 588 and 618 nm maybe related to the surface state. And the weak peak at 545 nm can be attributed to the interstitial sulfur states [48]. Besides the four similar peaks at 448, 460, 528 and 618 nm of ZnS-1, ZnS-2.5 has another four peaks at the wavelength of 501, 536, 556 and 582 nm. The weak emission peak at 501 nm and 556 nm should be associated with point defects, which are most likely the zinc vacancies [45,49]. And the peak at 536 nm is related to the interstitial sulfide [49], which maybe originated from the Na₂S oxidation by dissolved oxygen in the process of hydrothermal reaction. In addition, the peak located at 582 nm is attributed to the recombination between the interstitial zinc states and the zinc vacancies [38]. It can be observed that a large number of the zinc vacancies exist in these ZnS-X samples, and more zinc vacancies formed in

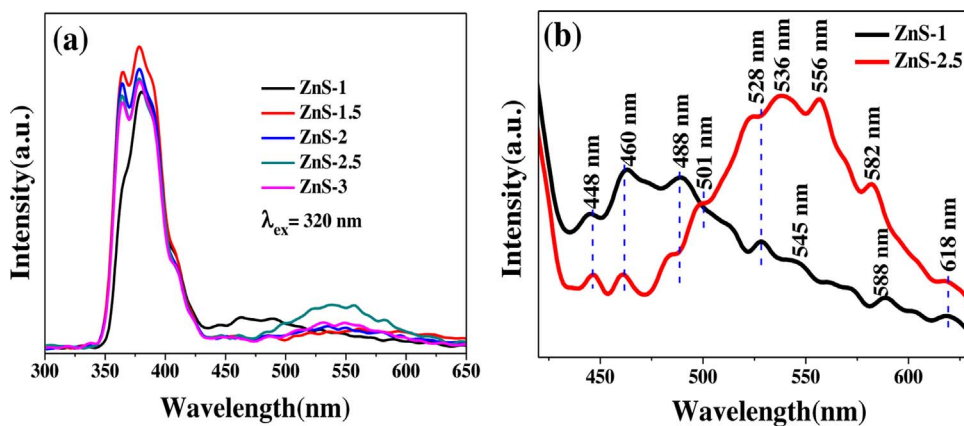


Fig. 4. Fluorescence spectra of the (a) ZnS-1, ZnS-1.5, ZnS-2, ZnS-2.5 and ZnS-3 samples and (b) ZnS-2.5 in the wavelength of 430 nm to 630 nm.

ZnS-2.5 than ZnS-1, this is in agreement with the XPS results. Furthermore, the broad emission peak shifts toward long wavelength for the samples with Zn:S mole ratio larger than 1:1, and the strongest emission intensity was obtained on ZnS-2.5. The Zn vacancy on sphalerite ZnS and wurtzite ZnS can be denoted as V_{Zn} and V_{WZn} , respectively. The wurtzite ZnS transform into the stable cubic phase ZnS results in the transformation of Zn vacancy type, which can be considered as V_{WZn} transform into the low energy V_{Zn} . Thus, with the increasing concentration of Zn vacancies and type changed, resulting in the light absorption enhanced and the emission peaks red shifted.

3.1.5. SEM and TEM characterization

The morphologies of ZnS-1 and ZnS-2.5 samples were examined by scanning electron microscope (SEM). As shown in Fig. 5a, the ZnS-1 particles have serious adhesiveness and amorphous agglomerations, which corresponds to the weak intensity in its XRD pattern. Compared with the ZnS-1 nanoparticles, the obtained ZnS-2.5 particles (Fig. 5b) are clearly observed to be larger irregular crystals, with some of them showing a cube shape. This result indicates that different $[\text{Zn}^{2+}/\text{S}^{2-}]$ has a distinct effect in regulating the sizes, morphology and crystallinity of the ZnS semiconductor. Particularly, the excess of Na_2S played a unique role on control of the sizes and crystallinity of ZnS. This result indicates that different $[\text{Zn}^{2+}/\text{S}^{2-}]$ has a distinct effect in regulating the sizes, morphology and crystallinity of the ZnS semiconductor. Particularly, the excess of Na_2S played a unique role on control of the sizes and crystallinity of ZnS.

The TEM images of the ZnS-1 sample (Fig. 6a) revealed that is a spherical-like nanoparticle, which size dimension is around 13.37 nm (Fig. S3). From the high-resolution TEM (HRTEM) image in Fig. 6b, the lattice fringes of ZnS-1 can be clearly observed in the yellow circle, and the lattice fringe spacing is 0.31 nm corresponds to the (002) plane of the wurtzite ZnS [11], which is agreement with the XRD and Raman results. In addition, we can observe that the lattice fringes are blurred and intermittent outside the yellow circle in Fig. 6b, indicating that is a

defects-rich region which resulted from the zinc vacancies. Apparently, an increased size of ZnS was observed with the content of Na_2S increasing. As shown in Fig. 6c-d, the ZnS-2.5 shows a large shell-like structure with a size dimension of around 274.2 nm (Fig. S4). The lattice fringes of ZnS-2.5 are clearly displayed in Fig. 6f, which testifies that is a well-defined crystal structure, and the spacing values of lattice fringes is 0.32 nm corresponds to the (111) plane of the sphalerite ZnS, which is well consistent with the XRD results. Moreover, the blurry lattice fringes are also observed in red circle region in Fig. 6f, suggesting there is abundance of zinc vacancies exist in the surface of ZnS-2.5 crystal, which is consistent with the XPS and PL results. This surface zinc vacancies could be attributed to the fact that excess of Na_2S with Zn^{2+} formed zinc deficient-ZnS, which disturbs the ZnS lattice in the surface. This surface zinc vacancies serve as holes trap that are beneficial to prevent the recombination of the photoinduced charges and enhance the electron transfer. And the blurry lattices fringes are also observed in the inside of the ZnS, indicating the zinc deficiency not only exist in surface but also in the subsurface of ZnS. Just as confirmed by XPS analysis, it is not a homogeneous distribution of zinc defects in bulk ZnS.

3.1.6. UV-vis diffuse reflectance absorption spectra (DRS) and Mott-Schottky analysis

To investigate the effect of the Zn vacancies on the optical/electronic of ZnS-X semiconductors, the UV-vis diffuse reflectance absorption spectra (DRS) and Mott-Schottky plots were investigated for the prepared ZnS-1, ZnS-1.5, ZnS-2, ZnS-2.5 and ZnS-3 samples. Fig. 7a shows UV-vis DRS for ZnS-X samples prepared with different amounts of Na_2S and the ZnS-X have three absorbance edges between 300 and 700 nm. All the ZnS-X samples absorb visible light can be clearly observed in the insert of Fig. 7a, indicating all of them have visible-light-induced photocatalytic activity, which originate from the defect states in their band structures. And a significant red-shift in the absorption edges are achieved with increasing content of Na_2S usage, indicating an

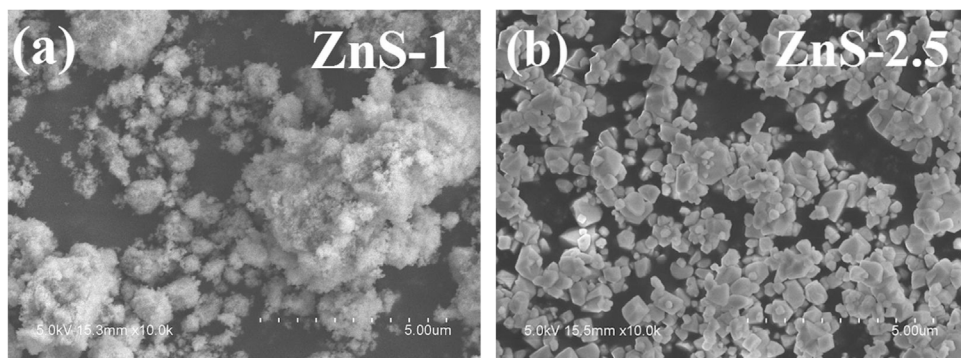


Fig. 5. SEM images of (a) ZnS-1 and (b) ZnS-2.5 samples.

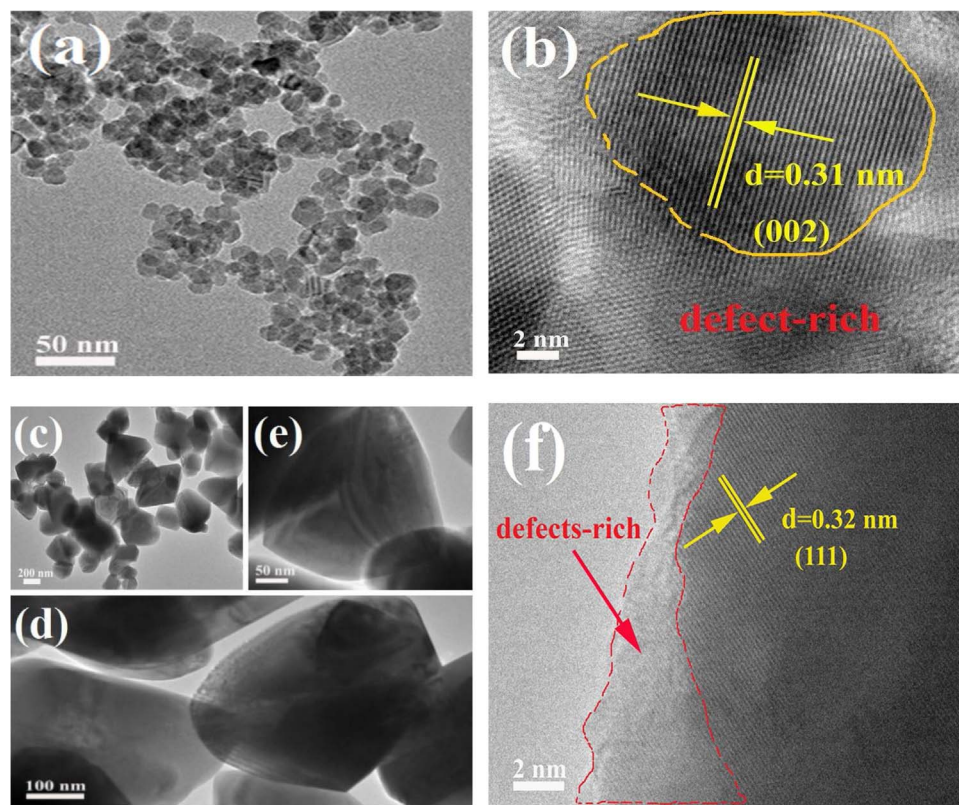


Fig. 6. TEM and HRTEM images of (a-b) ZnS-1 and (c-f) ZnS-2.5 samples.

increasing concentration of zinc vacancies in the ZnS-X. And the ZnS-3 sample exhibited higher absorption intensity than other four samples due to the larger amount of zinc deficiency. The corresponding main band structures of the ZnS-X samples (Fig. 7b) in visible light region are calculated by the transformed Kubelka-Munk function ($\alpha h\nu = A(h\nu - E_g)^{1/2}$, where α is the absorption coefficient, $h\nu$ is the photon energy, E_g is the direct band gap (eV), and A is a constant) [24]. It can be clearly observed that a progressively shifted up of Zn vacancy defect energy levels in ZnS-X bandgaps and the main bandgaps of ZnS-X are slightly changed with the amount of Zn vacancy increased except for ZnS-1 (the main bandgaps are 2.97, 3.45, 3.41, 3.34 and 3.29 eV for ZnS-1, ZnS-1.5, ZnS-2, ZnS-2.5 and ZnS-3, respectively). In addition, exception of the strong band-gaps in visible light region, all of ZnS-X have another weak absorption in the visible light region, suggesting that is not a homogeneous distribution of Zn defects in the bulk ZnS-X, and this is consistent with the TEM results. Apparently, with the increasing amount of Na₂S in precursor solution, the visible light response capability of as-prepared ZnS-X samples are increasing. This result indicating that varying amount of Na₂S can assist synthesis of Zn-

deficient ZnS with tunable band structures for efficient visible-light-driven photocatalytic reaction.

Mott – Schottky plots show that the flat-band potential (E_{FB}) of ZnS-X semiconductors were significantly affected by the introduction amount of zinc vacancies. Figs. 8 a and S5 display that all the linear plots possess positive slopes, which indicates the typical n-type semiconductor behavior of the ZnS-X photocatalysts. There is a negative shift in E_{FB} as the Na₂S increased during synthesis process, indicating an easy charge transfer process [37]. And the gradient of the plots increases can be attributed to the defect concentration increases [37], which led to an increasing visible-light photocatalytic activity. This is in agreement with the XPS and UV-vis DRS results. The E_{FB} are estimated to be −0.94, −1.05, −1.10, −1.16 and −1.19 V vs. SCE for ZnS-1, ZnS-1.5, ZnS-2, ZnS-2.5 and ZnS-3, respectively. Generally, the conduction band potentials (E_{CB}) for n-type semiconductor is more negative about −0.1 or −0.2 V than its flat band potential [50]. And thus, the E_{CB} for ZnS-1, ZnS-1.5, ZnS-2, ZnS-2.5 and ZnS-3 are roughly reckon up to be −1.14, −1.25, −1.30, −1.36 and −1.39 V vs. SCE, that is, −0.5, −0.61, −0.66, −0.72 and −0.75 V vs. normal hydrogen

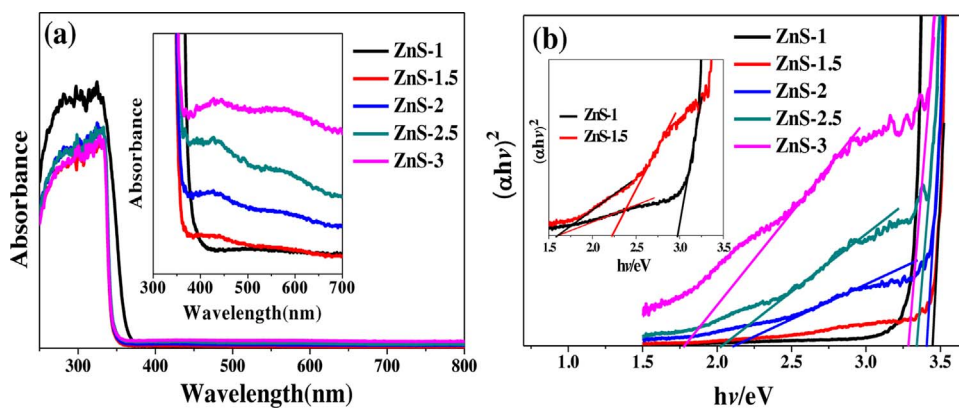
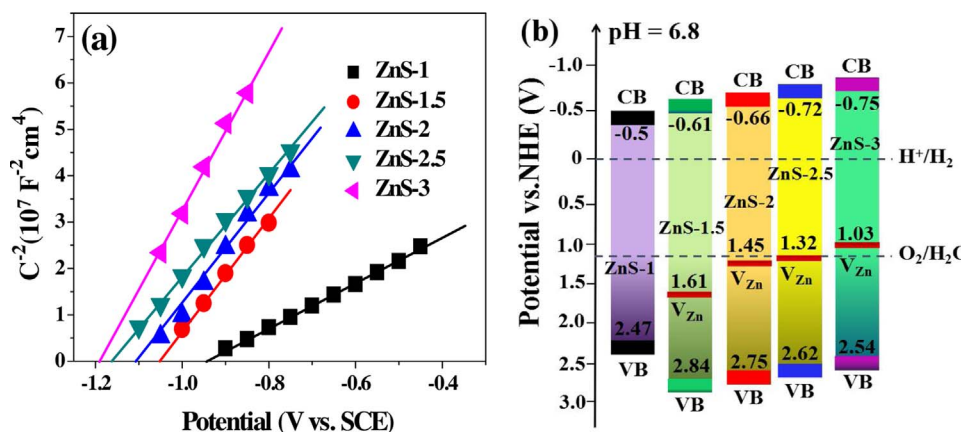


Fig. 7. (a) UV-vis DRS of ZnS-1, ZnS-1.5, ZnS-2, ZnS-2.5 and ZnS-3 samples. The insert is the corresponding magnified image which is from 300 nm to 800 nm. (b) The $(\alpha h\nu)^2$ versus $h\nu/eV$ curve of the ZnS-1, ZnS-1.5, ZnS-2, ZnS-2.5 and ZnS-3 samples.



electrode (NHE) ($E_{\text{NHE}} = E_{\text{SCE}} + 0.05916 \text{pH} + 0.241 \text{ V}$). The negative shift of E_{CB} suggests the reductive capacity enhanced for H_2/H^+ . Combined with the bandgap energy obtained by the UV-vis DRS results (Fig. 7b), the E_{VB} for ZnS-X are calculated by equation of $E_{\text{VB}} = E_{\text{CB}} + E_g$ [51]. More clearly, the band positions of E_{CB} and E_{VB} for the ZnS-X samples are schematically illustrated in Fig. 8b. It should be noted that, the zinc vacancies on ZnS-X samples created defect energy levels in their bandgaps and it at about 1.1 eV above the valence band in ZnS, which act as an acceptor levels for the photoinduced holes and weaken the oxidative capacity of the holes [37]. Thus, the positions of calculated zinc vacancies of ZnS-X in the band structure shift gradually from 1.61 V (ZnS-1.5) to 1.03 (ZnS-3), indicating introduction of zinc vacancies can significant reduction of the oxidative capacity of the holes and efficiently suppress the photocorrosion of ZnS (oxidation potential of S/ZnS is 0.28 V vs. NHE) [38]. As a result, an excellent photoreduced activity and a higher photostability are obtained.

3.2. Effect of molar ratio of Zn/S and concentration of sacrifice reagent on the photocatalytic activity of ZnS

The photocatalytic hydrogen evolution activities of the as-prepared ZnS-X photocatalysts were carried out in presence of 0.35 M Na_2S and 0.25 M Na_2SO_3 aqueous solution as sacrificial reagents under visible light irradiation ($\lambda \geq 420 \text{ nm}$). As shown in Fig. 9, Zn vacancies are crucial role for improving the photocatalytic H_2 evolution activity under visible light irradiation. As well-known, ZnS is not has photocatalytic activity under visible light irradiation because the wide bandgap (3.6 eV) [18,44]. The superior visible-light photocatalytic activities of ZnS-X catalysts can be attributed to their enhanced visible-

light absorption and excellent charge separation efficiencies caused by the Zn vacancies in the ZnS photocatalysts. In Fig. 9a, the rate of H_2 production for ZnS with different Zn/S molar ratio under visible light irradiation was depicted. It was found that the rate of H_2 evolution initially increases and then decline with an increasing amount of Na_2S in the precursor solution. The corresponding H_2 production rates are $83.77 \pm 2.60 \mu\text{mol h}^{-1} \text{ g}^{-1}$, $218.43 \pm 2.19 \mu\text{mol h}^{-1} \text{ g}^{-1}$, $296.36 \pm 3.88 \mu\text{mol h}^{-1} \text{ g}^{-1}$, $337.71 \pm 3.72 \mu\text{mol h}^{-1} \text{ g}^{-1}$ and $226.29 \pm 2.15 \mu\text{mol h}^{-1} \text{ g}^{-1}$, for the samples of ZnS-1, ZnS-1.5, ZnS-2, ZnS-2.5 and ZnS-3, respectively. The maximum rate of hydrogen evolution was observed for ZnS-2.5. As further increase in the amount of Na_2S results in a decrease of the rate for photocatalytic hydrogen generation, which is possibly due to the excessive amount of Zn vacancies in the ZnS. It's worth noting that, excessive amount of the defects can act as recombination centers leading to the recombination of photogenerated electrons and holes and hence decreasing the photocatalytic activity [36]. The results suggest that there might be an optimum concentration of Zn vacancies in ZnS for obtaining high photocatalytic activity. Therefore, controlling the amount of Zn defects is great important to photocatalytic reaction. All of the results indicate that Zn-deficient ZnS can be used as an efficient photocatalyst for photocatalytic H_2 evolution under visible light irradiation, and the Zn vacancies in ZnS play an important role in regulation the band gap and expand the visible light absorption range.

The concentrations of the sacrificial reagents had a significant influence on the photocatalytic activity. Fig. 9b displays the dependence of hydrogen production rate of ZnS-2.5 on the concentrations of the sacrificial reagents. Both low and high concentrations of the sacrificial reagent conditions are not conducive to hydrogen evolution. The

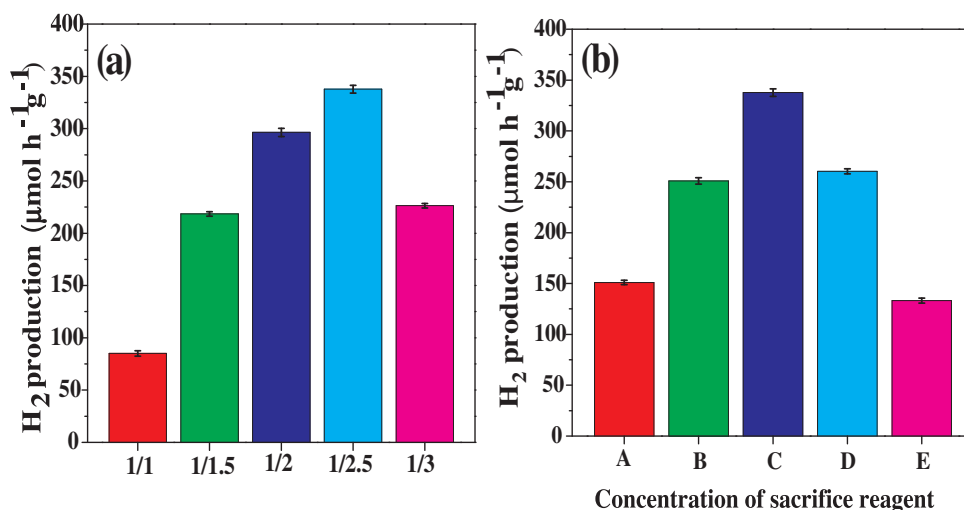


Fig. 9. (a) Hydrogen evolution rate of different Zn/S molar ratio of ZnS in 0.35 M Na_2S and 0.25 M Na_2SO_3 aqueous solution under visible light irradiation ($\lambda \geq 420 \text{ nm}$). The error bars in (a) represent the standard error of three independent experiments; (b) Photocatalytic H_2 evolution on ZnS-2.5 in presence of various concentrations of sacrificial reagents under visible light irradiation ($\lambda \geq 420 \text{ nm}$); A: 0.0875 M Na_2S , 0.0625 M Na_2SO_3 ; B: 0.175 M Na_2S , 0.125 M Na_2SO_3 ; C: 0.35 M Na_2S , 0.25 M Na_2SO_3 ; D: 0.525 M Na_2S , 0.375 M Na_2SO_3 ; E: 0.7 M Na_2S , 0.5 M Na_2SO_3 . (Reaction time: 5 h).

optimized photocatalytic activity of ZnS-2.5 was achieved in presence of 0.35 M Na₂S and 0.25 M Na₂SO₃ aqueous solution as sacrificial reagents in this photocatalysis system. When the concentration of Na₂S and Na₂SO₃ was fixed at 0.0875 M and 0.0625 M, the hydrogen production rate is only $151.03 \pm 2.04 \mu\text{mol h}^{-1} \text{g}^{-1}$. With the increase of sacrificial reagents concentration to four times (0.35 M Na₂S and 0.25 M Na₂SO₃), the highest hydrogen evolution rate of $337.71 \pm 2.15 \mu\text{mol h}^{-1} \text{g}^{-1}$ is obtained. Further increase of sacrificial reagents concentration led to an obviously decline for the hydrogen evolution rate. The reason is that a higher concentration of Na₂S leads to a higher pH value, which can affect the flat-band potential of the ZnS photocatalyst as well as the redox potential of H⁺/H₂ [16]. With the pH value increasing, the flat-band potential of ZnS becomes less negative leading to the decrease of photocatalytic activity [16]. Thus, an appropriate sacrificial reagents concentration is required to achieve the optimum hydrogen evolution rate.

3.3. Photocatalytic stability over ZnS-1 and ZnS-2.5 for H₂ evolution and recyclability

The photocatalytic stability of ZnS-1 and ZnS-2.5 for hydrogen evolution is evaluated using 0.35 M Na₂S and 0.25 M Na₂SO₃ aqueous solution as sacrificial reagents under visible light irradiation ($\lambda \geq 420 \text{ nm}$). As shown in Fig. 10a, the photocatalytic activity of as-prepared ZnS-1 is $408.25 \mu\text{mol g}^{-1}$ and deactivated beyond 5 h under visible light irradiation due to the strong photocorrosion. Compared with the ZnS-1, the zinc-deficient ZnS-2.5 with optimum amount of Zn vacancies shows superior photocatalytic activity for H₂ evolution that reach $2983.67 \mu\text{mol g}^{-1}$ under visible-light irradiation over 10 h and a much higher photostability is also obtained. The reason is that the Zn vacancies weaken oxidative capacity of holes to a large extent by raising the VB position, thus protect Zn-deficient ZnS-2.5 from photocorrosion. XRD patterns of the fresh and used ZnS-1 in Fig. S6a shows a slightly decrease in peak intensity, and the yellow color is clearly observed on the used ZnS, implying severe photocorrosion happened during the irradiation process for ZnS-1. For the ZnS-2.5, the XRD patterns (Fig. S6b) and the color of fresh and used sample have no notable differences, indicating that ZnS-2.5 is photostable. And no peak belong to elements sulfur is detected both in ZnS-1 and ZnS-2.5, it maybe the amount of elements sulfur is too little to be detected out. XPS spectra was used to further measurement the ZnS-1and ZnS-2.5 which are used for 10 h. Compared with the S 2p spectra of fresh and used ZnS-1(Fig. S7a and b), we can clearly observe that the peak attributed to S⁰ is significantly extending, the peak area ratio of S⁰ is 1: 8.75 for fresh and used ZnS-1, indicating the severe photocorrosion of ZnS-1 after 10 h irradiation. And the decreased surface atomic ratio of Zn: S in Table S2 is also testified the photocorrosion happened during the irradiation process for ZnS-1. As for the ZnS-2.5, both the elements sulfur peak (Fig. S7c and d) and surface atomic ratio of Zn:S (Table S2) are clearly proved that no photocorrosion happened during the irradiation

process. These results indicate that Zn-deficient ZnS-2.5 can be used as a stable photocatalyst for visible-light-driven H₂ production from water.

We further investigate the recyclability of ZnS-2.5 and ZnS-1 over four runs of totally 20 h, and the results are shown in Fig. 10b. It was observed that in the first run, the maximum amounts of photocatalytic H₂ evolution of ZnS-2.5 is $1685.6 \mu\text{mol g}^{-1}$, whereas ZnS-1 has visible light activity only in the first 5 h. In the second, third and fourth run, the amounts of photocatalytic H₂ evolution for ZnS-2.5 slightly declined one by one. The reason is that the Zn-deficient ZnS-2.5 still exist slight photocorrosion under long time irradiation, thus resulting in visible-light activity gradually reduced, but it still as a robust photocatalyst for continuous H₂ production under visible light irradiation compared with ZnS-1. This results further indicating the Zn vacancies can significantly suppress the photocorrosion and enhance the photostability. XRD results of the fresh and used ZnS-2.5 sample (Fig. S8) have no notable differences, and no peak belong to elements sulfur is detected, implying that ZnS-2.5 is photostable in some degree. These results indicate that Zn-deficient ZnS-2.5 can be used as a stable photocatalyst for visible-light-driven H₂ production from water.

In addition, the visible-light photocatalytic activity and photostability of ZnS-2.5 which is prepared with other different sulfur sources (such as thiourea (THU) and thioacetamide (TAA)) is also investigated. As shown in Fig. S9, when the TAA as sulfur source, the as-prepared ZnS has a very low visible-light photocatalytic activity of $156.58 \mu\text{mol g}^{-1}$ and it is inactive after 4 h; when THU was used as sulfur source, it also has a low activity and photostability, and the visible-light photocatalytic activity of ZnS is only $446.19 \mu\text{mol g}^{-1}$ over 10 h. But when the Na₂S as sulfur source, the photocatalytic activity for H₂ evolution reach $2983.67 \mu\text{mol g}^{-1}$ under visible-light irradiation over 10 h. The photocatalytic activity is 19.06 times and 6.69 times higher than that of the TAA and THU as sulfur source, respectively. The result suggests that Na₂S is a better sulfur source to prepare the zinc deficient-ZnS for enhancing the visible-light photocatalytic activity.

3.4. Electrochemical analysis

To prove the important role of Zn vacancies in facilitating the transfer of photogenerated electrons and separation of charges, the Nyquist plots of electrochemical impedance spectroscopy (EIS) are performed in dark. As presented in Fig. 11a, each impedance spectrum consist of a semicircle arc at the high frequency range and a straight line at the low-frequency region for ZnS-X samples. And compared with those of samples, the plots of ZnS-2.5 at the lower frequency region represent it has a better conductivity [52]. Further, this phenomenon proves the lower recombination rate of charges and fast electron transfer in ZnS-2.5 due to its optimum amount of Zn vacancies. This results further confirming that increasing the content of Na₂S in synthesis can introduce more surface Zn vacancies on ZnS-X, which is highly beneficial for the charge transfer (with the exception being ZnS-3 which may be caused by its excessive Zn defects).

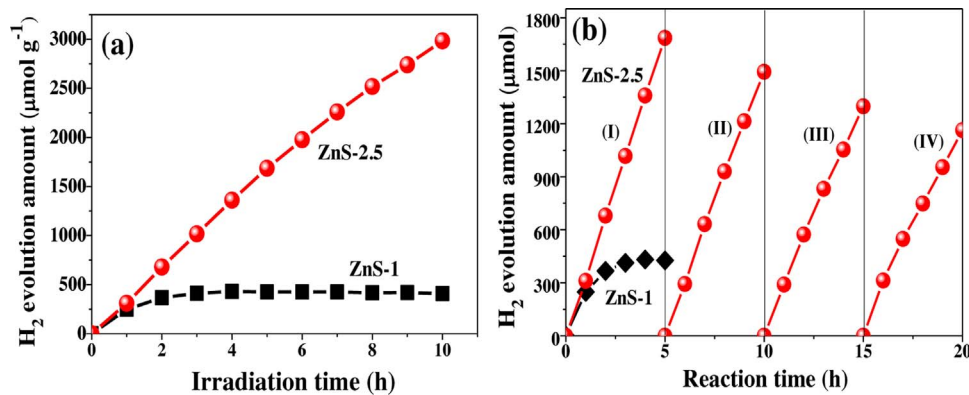
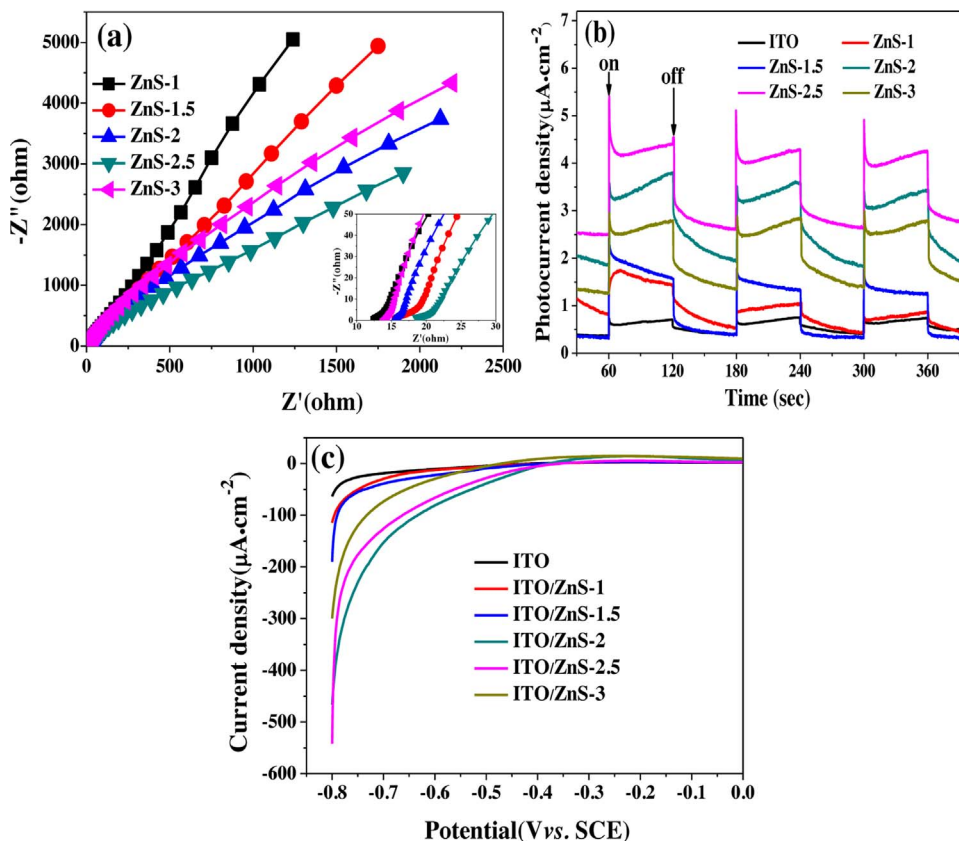


Fig. 10. (a) The photocatalytic stability of ZnS-1 and ZnS-2 photocatalysts for hydrogen evolution under visible light irradiation ($\lambda \geq 420 \text{ nm}$). (b) Recyclability testing and comparison of H₂ evolution over ZnS-1 and ZnS-2.5 in 0.35 M Na₂S and 0.25 M Na₂SO₃ aqueous solution as sacrificial reagents.



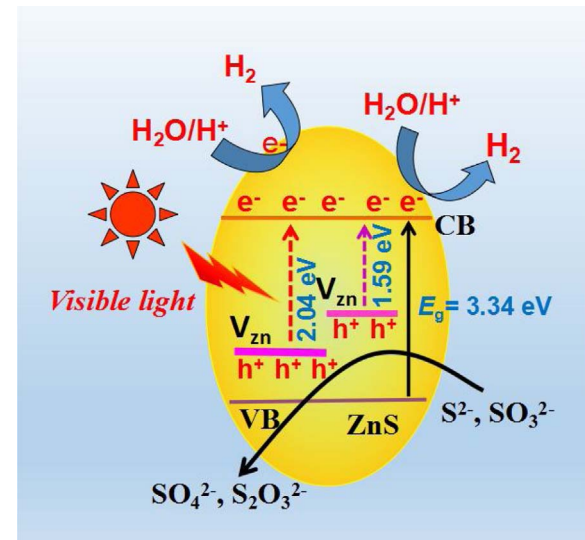
Transient photocurrent measurements of ZnS-1, ZnS-1.5, ZnS-2, ZnS-2.5 and ZnS-3 samples revealed that ZnS-X exhibited a sensitive photocurrent response during several on-off cycles of intermittent irradiation under visible light. As shown in Fig. 11b, the photocurrent intensities of these ZnS-X samples are in accordance with the trend seen in their photocatalytic H₂ evolution activities. The ZnS-2.5 shows the highest photocurrent intensity under visible light irradiation in these five samples, which reflects a better visible-light response and more efficient photoexcited charge separation, whereas the lowest photocurrent intensity can be observed in the ZnS-1 sample. This result additionally indicates the visible-light photocatalytic activity of the ZnS can be attributed to the Zn vacancies, which greatly improved the visible light response and charge separation efficiency. As a result, a high photocatalytic H₂ evolution activity for ZnS under visible light irradiation is achieved.

In addition, the electrochemical H₂ evolution activities of ZnS-1, ZnS-1.5, ZnS-2, ZnS-2.5 and ZnS-3 electrodes are also measured by the linear sweep voltammetry (LSV) technique. As shown in Fig. 11c, the cathodic current related to the reduction of water to H₂ on bare ITO electrode was extremely low even at high applied potentials, whereas ITO/ZnS-1, ITO/ZnS-1.5, ITO/ZnS-2, ITO/ZnS-2.5 and ITO/ZnS-3 electrodes showed an increased cathodic current at the same potential range and the much higher current density and low over-potential measured for ITO/ZnS-2.5 electrode, which clearly indicating the increased electron migration with optimized amount of Zn vacancies compared with that of other four samples [53].

3.5. The mechanism for H₂ evolution

On the basis of above results, the photocatalytic mechanism for H₂ production over Zn-deficient ZnS-2.5 under visible light irradiation can be depicted in Scheme 1. The much higher visible-light photocatalytic H₂ evolution activity of ZnS-2.5 is attributed to the introduced Zn vacancies which created defect energy levels in the bandgap, thus

Fig. 11. (a) EIS Nyquist plots of ZnS-1, ZnS-1.5, ZnS-2, ZnS-2.5 and ZnS-3 samples coated on ITO measured at 0.5 V vs. SCE in a 0.5 M Na₂SO₄ aqueous solution; (b) Transient photocurrent response for the ZnS-1, ZnS-1.5, ZnS-2, ZnS-2.5 and ZnS-3 in 0.5 M Na₂SO₄ aqueous solution under visible light irradiation ($\lambda \geq 420$ nm); (c) LSV curves of ZnS-1, ZnS-1.5, ZnS-2, ZnS-2.5 and ZnS-3 in 0.5 M Na₂SO₄ aqueous solution. The scan rate is 5 mV s⁻¹.



Scheme 1. Photocatalytic mechanism for H₂ production over Zn-deficient ZnS-2.5 under visible light irradiation.

enhanced the visible-light photocatalytic response and improved charge carrier separation. Under visible light irradiation, the Zn-deficient ZnS-2.5 can be photoexcited because the Zn vacancies narrow energy band gap which produces defect energy levels. This can enhance visible-light absorption and the photoinduced electrons and holes separation rate. The photoinduced electrons direct transfer to the CB of ZnS and then reduction of H⁺ to produce H₂. Compared with ZnS-1, the up-shifted E_{CB} for ZnS-2.5 enables the reductive capacity of photoinduced electrons enhanced for H₂/H⁺. In addition, the Zn vacancies weaken oxidative capacity of holes to a large extent by raising the VB position and protected Zn-deficient ZnS from photocorrosion. Hence, the

photostability and visible light photocatalytic activity of ZnS-2.5 for hydrogen production are remarkably enhanced. It is therefore concluded that introducing defect states have great potential to modify photocatalysts for efficient photocatalytic hydrogen evolution.

4. Conclusions

In summary, zinc defects are successfully introduced into ZnS via adding sodium sulfide as sulfur source during the hydrothermal treatment. The density of zinc vacancies on ZnS samples are regulated by varying the amount of sodium sulfide usage. Triple roles of the zinc vacancies in defective ZnS are displayed, acting as photosensitization units that induce visible light response and as an acceptor levels for the photoinduced holes that improve charge carrier separation rate, and raising the VB position that weaken the oxidative capacity of the holes to protect Zn-deficient ZnS from photocorrsion. Thereby, due to enhanced visible-light absorption and improved charge carrier separation, the Zn-deficient ZnS-2.5 exhibited superior photocatalytic hydrogen evolution activity that reaches $337.12 \mu\text{mol h}^{-1} \text{g}^{-1}$ under visible light irradiation. Furthermore, the photocatalytic activities of Zn-deficient ZnS for H_2 production increase with increasing the amount of Zn vacancies until it reaches the optimum value, but decrease sharply when it goes beyond the optimum value because excessive amount of Zn vacancies act as recombination centers of photogenerated electrons and holes. This work present a simple and highly effective strategy for intrinsic modification of ZnS by self-defects for achieving practical visible-light photocatalysis and improving solar energy capture and conversion.

Acknowledgements

This work was financially supported by NSFC (21773113, 21273106, 21273111 and 51272101), the Jiangsu Provincial Natural Science Foundation (No.BK20130053, BK20151265, BK20150396). The authors would like to thank Analysis Center of Nanjing University for the sample characterization.

Appendix A. Supplementary data

Supplementary data associated with this article can be found, in the online version, at <http://dx.doi.org/10.1016/j.apcatb.2017.09.006>.

References

[1] J. Chen, D. Yang, D. Song, et al., *J. Power Sources* 280 (2015) 649–666.

- [2] L. Yuan, C. Han, M.Q. Yang, et al., *Int. Rev. Phys. Chem.* 35 (2016) 1–36.
- [3] Y. Shi, B. Zhang, *Chem. Soc. Rev.* 45 (2016) 1529–1541.
- [4] X. Chen, S. Shen, L. Guo, et al., *Chem. Soc. Rev.* 110 (2010) 6503–6570.
- [5] J. Ran, J. Zhang, J. Yu, et al., *Chem. Soc. Rev.* 43 (2014) 7787–7812.
- [6] B. Qiu, Q. Zhu, M. Du, et al., *Chem. Int. Ed.* 129 (2017) 2728–2732.
- [7] B. Qiu, Q. Zhu, M. Xing, et al., *Chem. Commun.* 53 (2017) 897–900.
- [8] J. Yuan, J. Wen, Q. Gao, et al., *Dalton Trans.* 44 (2015) 1680–1689.
- [9] G. Wang, B. Huang, Z. Li, *Sci. Rep.* 5 (2015).
- [10] J.S. Hu, et al., *Angew. Chem. Int. Ed.* 44 (2005) 1269–1273.
- [11] J. Zhang, et al., *Nano Lett.* 11 (2011) 4774–4779.
- [12] G.J. Lee, S. Anandan, S.J. Masten, et al., *Renew. Energy* 89 (2016) 18–26.
- [13] T. Arai, S. Senda, Y. Sato, et al., *Chem. Mater.* 20 (2008) 1997–2000.
- [14] Y. Wang, J. Wu, J. Zheng, et al., *Catal. Sci. Technol.* 1 (2011) 940–947.
- [15] D.H. Wang, L. Wang, A.W. Xu, *Nanoscale* 4 (2012) 2046–2053.
- [16] Y. Wang, J. Wu, J. Zheng, et al., *Catal. Sci. Technol.* 2 (2012) 581–588.
- [17] M. Muruganandham, Y.J. Kusumoto, *Phys. Chem. C* 113 (2009) 16144–16150.
- [18] Y. Zhou, G. Chen, Y. Yu, et al., *Phys. Chem. Chem. Phys.* 17 (2015) 1870–1876.
- [19] J. Zhang, Y. Wang, J. Zhang, et al., *ACS Appl. Mater. Interfaces* 5 (2013) 1031–1037.
- [20] Z. Shen, G. Chen, Q. Wang, et al., *Nanoscale* 4 (2012) 2010–2017.
- [21] S. Zhao, J. Huang, Q. Huo, et al., *J. Mater. Chem. A* 4 (2016) 193–199.
- [22] Z. Fang, S. Weng, X. Ye, et al., *ACS Appl. Mater. Interfaces* 7 (2015) 13915–13924.
- [23] K. Li, R. Chen, S.L. Li, et al., *Chem. Sci.* 6 (2015) 5263–5268.
- [24] Y. Xia, Q. Li, K. Lv, et al., *Appl. Catal. B: Environ.* 206 (2017) 344–352.
- [25] W. Zhang, Z.Y. Zhong, Y.S. Wang, R.J. Xu, *Phys. Chem. C* 112 (2008) 17635–17642.
- [26] G. Liu, et al., *J. Phys. Chem. C* 113 (2009) 21784–21788.
- [27] M. Kong, et al., *J. Am. Chem. Soc.* 133 (2011) 16414–16417.
- [28] J.P. Wang, et al., *ACS Appl. Mater. Interfaces* 4 (2012) 4024–4030.
- [29] Y.H. Lv, et al., *Catal. Sci. Technol.* 3 (2013) 3136–3146.
- [30] P. Wang, D. Wang, J. Lin, et al., *ACS Appl. Mater. Interfaces* 4 (2012) 2295–2302.
- [31] M.L. Guang, et al., *J. Am. Chem. Soc.* 135 (2013) 10411–10417.
- [32] P. Niu, G. Liu, H.M.J. Cheng, *Phys. Chem. C* 116 (2012) 11013–11018.
- [33] Z. Hong, B. Shen, Y. Chen, et al., *J. Mater. Chem. A* 1 (2013) 11754–11761.
- [34] P. Niu, L.C. Yin, Y.Q. Yang, et al., *Adv. Mater.* 26 (2014) 8046–8052.
- [35] H. Yu, R. Shi, Y. Zhao, et al., *Adv. Mater.* 29 (2017) 201605148.
- [36] G. Wang, B. Huang, Z. Li, et al., *Sci. Rep.* 5 (2015).
- [37] F. Kurnia, Y.H. Ng, R. Amal, et al., *Solar Energy Mater. Solar C* 153 (2016) 179–185.
- [38] T. Mahvelati-Shamsabadi, E.K. Goharshadi, *Ultrasound. Sonochem.* 34 (2017) 78–89.
- [39] X. Yu, J. Yu, B. Cheng, et al., *Chem. Eur. J.* 15 (2009) 6731–6739.
- [40] F. Huang, J.F. Banfield, *J. Am. Chem. Soc.* 127 (2005) 4523–4529.
- [41] C.A. Arguello, D.L. Rousseau, S.P.S. Porto, *Phys. Rev.* 181 (1969) 1351.
- [42] O. Brafman, S.S. Mitra, *Phys. Rev.* 171 (1968) 931.
- [43] Y.C. Cheng, C.Q. Jin, F. Gao, et al., *J. Appl. Phys.* 106 (2009) 123505.
- [44] D. Jiang, Z. Sun, H. Jia, et al., *J. Mater. Chem. A* 4 (2016) 675–683.
- [45] M. Salavati-Niasari, M.R. Loghman-Estarki, F. Davar, *J. Alloy Compd.* 475 (2009) 782–788.
- [46] Y. Li, Y.J. Wu, *Am. Ceram. Soc.* 98 (2015) 2972–2975.
- [47] W. Zhang, X. Zeng, H. Liu, et al., *J. Lumin.* 134 (2013) 498–503.
- [48] B. Soenen, J. Van den Bossche, P. De Visschere, *J. Appl. Phys.* 82 (1997) 5241.
- [49] T. Mitsui, Y. Yamamoto, *J. Appl. Phys.* 80 (1996) 6972.
- [50] S.S. Yi, J.M. Yan, B.R. Wulan, et al., *Appl. Catal. B: Environ.* 200 (2017) 477–483.
- [51] L.J. Zhang, S. Li, B.K. Liu, et al., *ACS Catal.* 4 (2014) 3724–3729.
- [52] X. Hao, Z. Jin, H. Yang, et al., *Appl. Catal. B: Environ.* 210 (2017) 45–56.
- [53] H. Zhao, P. Jiang, W. Cai, *J. Chem. Asian* 12 (2017) 361–365.